Earth, Planets and Space

FULL PAPER Open Access

Relationship between the low-latitude coronal hole area, solar wind velocity, and geomagnetic activity during solar cycles 23 and 24

Yumi Nakagawa[1*], Satoshi Nozawa[2] and Atsuki Shinbori[3]

Abstract

In order to statistically investigate the relationship between the low-latitude coronal holes (CHs), the solar wind speed, and the geomagnetic activity in solar cycles 23 (1996–2008) and 24 (2009–2016), we conducted a superposed epoch analysis of the variations in CH area, solar winds, the interplanetary magnetic field (IMF), and geomagnetic indices (AL, AU, and SYM-H) for the period from 1996 to 2016. We further divided the temporal variations of the IMF into four types and then investigated the variations in solar winds, the IMF, and the geomagnetic indices before and after the corotating interaction region (CIR) reached Earth's magnetosphere in each case. As a result, we observed a north–south asymmetry in the CH area, which shows that the CH area was much larger in the southern hemisphere than in the northern hemisphere during solar cycles 23 and 24. In addition, the CH area for solar cycle 24 tended to appear in a wider latitude region compared with that for solar cycle 23. The maximum values of the CH area and the solar wind speed in solar cycle 24 tended to be smaller than those in solar cycle 23. The relationship between these maximum values showed a positive correlation for both solar cycles. The distribution was larger for solar cycle 23 than for solar cycle 24. The variations in solar wind speed and the geomagnetic indices (AE and SYM-H) associated with CIRs in solar cycle 24 tended to be smaller than those in solar cycle 23. We conclude that the geomagnetic activity for solar cycle 24 associated with CIRs was slightly lower compared with that for solar cycle 23. This decrease in geomagnetic activity was due to a decrease in the dawn-to-dusk solar wind electric field intensity, which is obtained as the product of the solar wind speed and the north–south component of the solar wind magnetic field.

Keywords: Space weather, CIR, Coronal hole, Solar wind, Geomagnetic activity

Introduction

Space weather refers to the conditions on the Sun and in solar wind, the magnetosphere, the ionosphere, and the thermosphere that can affect the performance and reliability of space-borne and ground-based technological systems and that can affect human life and health (Schwenn 2006). Disturbances in space weather affect human life by causing, for example, artificial satellite failure, communication problems, and astronaut exposure. Therefore, it is necessary to predict their magnitude and duration.

Many studies have shown that the solar activity for solar cycle 24 is low [e.g., Jiang et al. (2007), Kamide and Kusano (2013) and Watari et al. (2015)]. Svalgaard et al. (2005) predicted that the then-approaching solar cycle 24 would have a peak smoothed monthly sunspot number of 75 ± 8 and that it may be the smallest cycle in the past 100 years. After that, the maximum sunspot number (SSN) recorded was 116.4 according to the World Data Center for Sunspot Index and Long-term Solar Observation (WDC-SILSO), Royal Observatory of Belgium, Brussels. This was the smallest number observed since the maximum of solar cycle 14 (Watari 2017). Gopalswamy

*Correspondence: 15nd406s@vc.ibaraki.ac.jp
[1] Graduate School of Evolution of the Universe and Earth, Ibaraki University, 2-1-1, Bunkyo, Mito 310-8512, Japan
Full list of author information is available at the end of the article

et al. (2015a) showed that high-solar-energy particle events were the lowest since the dawn of the space age. From the viewpoint of space weather, it is important to investigate the differences in scale between solar activity and geomagnetic activity in solar cycles 23 and 24.

Solar phenomena that are a key factor for variations in space weather are coronal holes (CH). CHs are dark regions in the solar corona and are frequently observed in the declining phase of each solar cycle. These features can be seen in extreme ultraviolet (EUV) and soft X-ray solar observations. The temperature and plasma density in the CH region are lower than those of the surrounding solar corona. High-speed solar wind can flow out from the CH region because it has open magnetic fields expanding into the interplanetary space. High-speed solar wind overtakes low-speed solar wind, and thus, the plasma density and magnetic field are compressed in a boundary between the high- and low-speed solar winds. When this solar wind structure, called corotating interaction region (CIR), arrives at Earth's magnetosphere, geomagnetic activity is frequently enhanced and the plasma environment in the magnetosphere is changed. Therefore, investigations of the characteristics of CHs and the CIR are essential for evaluating the influence of the Sun on the environment in geospace.

There have been many previous studies on the characteristics of plasma environmental changes in the magnetosphere and the ionosphere due to high-speed solar winds with a CH origin [e.g., Harvey and Sheeley (1978), Sheeley and Harvey (1981) and Verbanac et al. (2011a, b)]. Harvey et al. (2000) and Harvey and Recely (2002) provided a good idea of the geoeffectiveness of high-speed solar wind flows during solar cycles. Harvey and Recely (2002) measured polar CHs from 1989 to 2002. They found that the pole hole is asymmetric around the pole and usually has lobes that frequently extend to the latitude of the active area. Because they focused on the long-term variation in polar CHs, Tsurutani et al. (2006b) suggested that the effects of isolated equatorial CHs should also be evaluated. Gopalswamy et al. (2015b) pointed out that polar CHs are an index of the strength of the polar magnetic field and the level of the activity of the next solar cycle (Gopalswamy et al. 2012; Selhorst et al. 2011; Shibasaki 2013; Mordvinov and Yazev 2014; Altrock 2014) and that equatorial CHs are a good indicator of high-speed streams (HSS) and CIRs reaching the earth (Tsurutani et al. 1995, 2006a; Cranmer 2009; Verbanac et al. 2011a; Akiyama et al. 2013; Borovsky and Denton 2013).

In addition to CIRs, coronal mass ejections (CMEs) also significantly change the plasma environment in the magnetosphere and the ionosphere. However, it is known that the influences of CIRs and CMEs on geomagnetic activity are different from each other. Borovsky and Denton (2006) showed that the response of the bow shock, the magnetosheath, the radiation belts, the ring current, the aurora, Earth's plasma sheet, magnetospheric convection, ULF pulsations, spacecrafts charging in the magnetosphere, and the saturation of the polar cap potential are different between CME-driven geomagnetic storms and CIR-driven geomagnetic storms. They also pointed out that CME-driven storms represent a more serious problem to Earth-based electrical system, whereas CIR-driven storms cause more problems for space-based assets.

There is a relationship between the CH area, high-speed stream (HSS)/CIR parameters, and geomagnetic indices (Verbanac et al. 2011b). Alves et al. (2006) investigated the effects of 727 CIRs on the magnetosphere from 1964 to 2003 by classifying the magnitude of the magnetic storm into three levels according to the value of the Dst index. They found that 33% of the CIRs induced moderate/intense magnetic activity ($Dst < -50$ nT). Zhang et al. (2008) investigated the effects of CIRs in the heliosphere (< 1 AU) on geomagnetic activity during solar cycle 23 (1996–2005) and found that 50% of the CIRs generate classical interplanetary shocks during the descent period and that 89% of CIR-related shocks are followed by a geomagnetic storm. These results show that CIR-related shocks are not a necessary condition for generating a magnetic storm, but the majority of CIR-related shocks are related to storms. Verbanac et al. (2011a) conducted a cross-correlation analysis of the fractional CHs area measured in the central meridian distance interval $\pm 10°$, solar wind velocity, the interplanetary magnetic field, and geomagnetic indices, and then showed that the Ap and AE indices exhibit a good correlation with CH area and solar wind parameters. Tokumaru et al. (2017) researched the relation between CH area and solar wind speeds during 1995–2011. They carried out a potential field (PF) model analysis of magnetograph observations and interplanetary scintillation (IPS) observations made by the Institute for Space-Earth Environmental Research (formerly the Solar Terrestrial Environment Laboratory) of Nagoya University and obtained a positive correlation between the square root of CH area and solar wind speed.

Recently, there have been many studies regarding the latitude of appearance of CHs for solar cycles 23 and 24. McIntosh et al. (2015) showed that the variations in the 50-day running average of CH area in the southern hemisphere were larger than those in the northern hemisphere from 1996 to 2008, which correspond to solar cycle 23, expect for 2004–2005 (see Fig. 6 in McIntosh et al. 2015). Abunina et al. (2015) categorized more than 300 CHs observed from 2002 to 2013 by their polarity and heliolatitude and showed that transequatorial holes,

northern holes with negative polarity, and southern holes with positive polarity produced more enhanced geomagnetic activity than the other holes. Lowder et al. (2016) detected CH areas for the period from May 31, 1996 to October 14, 2014 by using SOHO/EIT195 Å and SDO/AIA193 Å data and showed that the latitude distribution of the appearance of CHs in the southern hemisphere was larger than that in the northern hemisphere during 1996–2008, whereas CH distribution after 2009 was smaller than that for solar cycle 23 (refer to Figs. 2 and 3 in Lowder et al. 2016). Bagashvili et al. (2017) investigated the area and latitude of appearance of 3056 CHs by calculating the rotational velocities of CHs from the position of the geometric center of a polygon for each object from January 1, 2013 to April 20, 2015, which includes the extended peak of solar cycle 24. In that study, CHs were divided into three groups according to their area and the researchers found that the distribution of CHs larger than 40,000 Mm^2 was concentrated around a latitude of $-60°$.

However, the latitudinal dependence of CH area on the magnitude of high-speed solar winds and geomagnetic activity remains unknown, and the differences in the responses of Earth's magnetosphere to high-speed solar winds between solar cycles 23 and 24 have not been clarified yet. The purpose of this study is to statistically investigate the relationship between low-latitude CHs, solar wind speeds, and geomagnetic activity for solar cycles 23 (1996–2008) and 24 (2009–2016). In the present study, we determine the CH area on the solar surface using two-dimensional soft 195 Å and 193 Å images obtained from SOHO/EIT and SDO/AIA and statistically investigate the variations in CH area, solar wind parameters, and geomagnetic activity indices.

Data set

We used the two-dimensional soft X-ray images obtained from the Extreme ultraviolet Imaging Telescope (EIT: Delaboudinière et al. 1995) onboard the Solar and Heliospheric Observatory (SOHO) and from the Atmospheric Imaging Assembly (AIA) onboard the Solar Dynamics Observatory (SDO: Lemen et al. 2012) in order to investigate the temporal and spatial variations in CH area on the solar surface. The EIT and AIA data were provided by the Virtual Solar Observatory (https://sdac.virtualsolar.org/cgi/search/) and AIA Cutoff Data (https://www.lmsal.com/get_aia_data/). The periods of the EIT and AIA data used in our analyses are from 1996 to 2008 and from 2009 to 2016, respectively. These data are calibrated, and the spatial resolution of the EIT and AIA data is 1024×1024 and 4096×4096, respectively. Furthermore, the solar wind proton density and flow speed, the interplanetary magnetic field (IMF), and geomagnetic indices (AU, AL, and SYM-H) were used to examine the response of the magnetosphere to the high-speed solar winds associated with CIRs. The time resolution of these data is 1 min. The IMF coordinates are expressed in geocentric solar magnetospheric (GSM) coordinates. The solar wind data and geomagnetic indices were provided by the Coordinated Data Analysis Web (CDAWeb: https://cdaweb.sci.gsfc.nasa.gov/) and by the World Data Center for Geomagnetism, Kyoto (WDC, Kyoto: http://wdc.kugi.kyoto-u.ac.jp/), respectively. In this study, we took advantage of the Inter-university Upper atmosphere Global Observation NETwork (IUGONET) data analysis web service (http://search.iugonet.org/list.jsp) and the IUGONET data analysis software (UDAS) (Tanaka et al. 2013) for ground-based observations of the upper atmosphere developed in the IUGONET project (Hayashi et al. 2013).

Analysis method

How to choose CIR events and the superposed epoch analysis method

In present study, we referred to the stream interaction region (SIR) and CIR lists based on observations by the Advanced Composition Explorer (ACE) and WIND from 1995 to 2009 (http://www-ssc.igpp.ucla.edu/~jlan/ACE/Level3/SIR_List_from_Lan_Jian.pdf, see Jian et al. (2006, 2011) for details) and the SIR lists based on the observations made at Solar TErrestrial RElations Observatory (STEREO) from 2010 to 2016 (http://wwwssc.igpp.ucla.edu/~jlan/STEREO/Level3/STEREO_Level3_SIR.pdf, refer to Jian et al. (2013) for details). SIRs are essentially the same as CIRs (Jian et al., 2011). From 1996 to 2009, we chose events in which low- and middle-latitude CHs were observed on the sun surface four days before the date of each CIR in the list. From 2010 to 2016, we referred to the solar wind density, flow speed, and the IMF around the date of each SIR in the list and visually extracted the date in which the solar wind density become maximum and the speed began to increase owing to the CIR's (or SIR's) arrival at Earth's orbit. Then, we chose events in which low- and middle-latitude CHs were observed on the sun surface 4 days before the date of each of the extracted events. As a result, we found 313 CIR events with low- and middle-latitude CHs in a period of 21 years. The number of CIR events found every 2 years and for all years is listed in Table 1. The italic letter represents the number of events analyzed in present study.

We conducted a superposed epoch analysis of the CH area, solar winds, the IMF, and geomagnetic indices in order to investigate the relationship between CH area, high-speed solar winds of CH origin, and geomagnetic activity. Figure 1 shows the variation of the

Table 1 The number of events every 2 years and all year in referred CIR/SIR list and the present study

Solar cycle 23			Solar cycle 24		
	Number of events in referenced list	Number of events in present analysis		Number of events in referenced list	Number of events in present analysis
1996–1997	57	*23*	2009–2010	74	*27*
1998–1999	41	*14*	2011–2012	75	*21*
2000–2001	36	*20*	2013–2014	59	*28*
2002–2003	45	*33*	2015–2016	65	*36*
2004–2005	52	*34*	–	–	–
2006–2007	80	*51*		–	–
2008	35	*26*		–	–
Total	346	*201*	Total	273	*112*

The italic letter represents the number of events analyzed in our study. The number of referenced SIR events rather than that of CIR is counted from 2010 to 2016

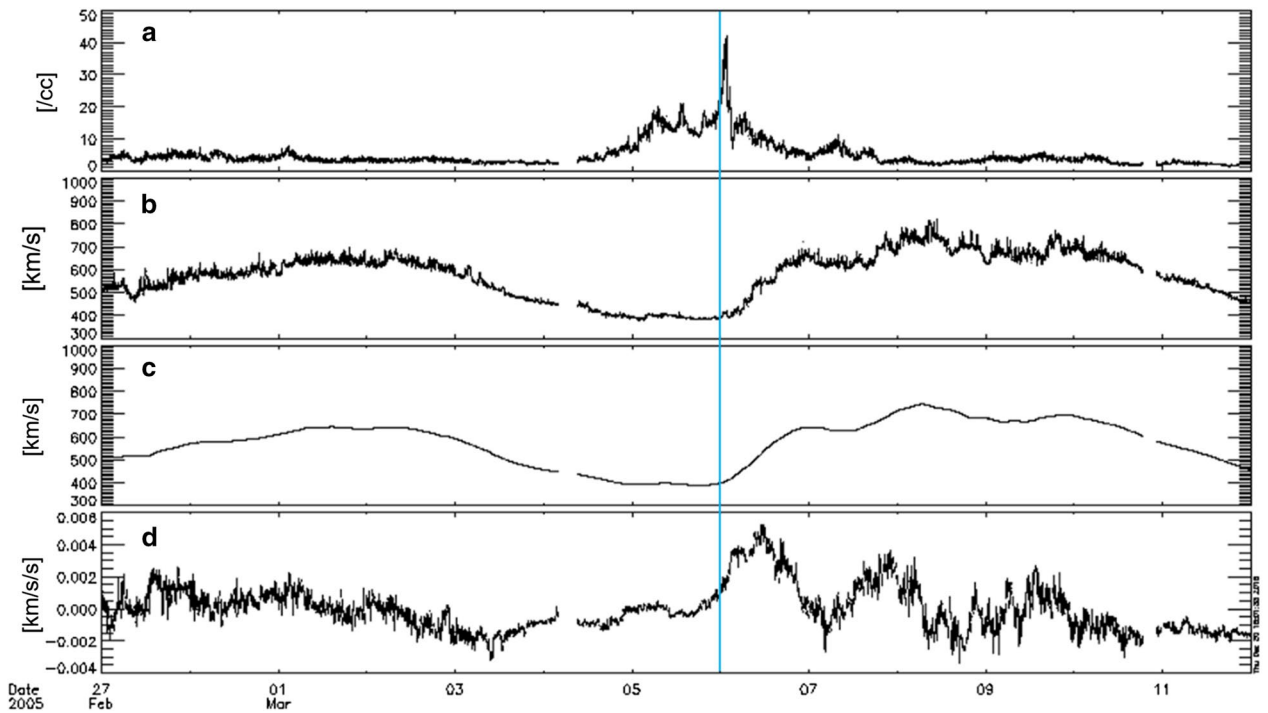

Fig. 1 The variations of the solar wind proton density and flow speed provided by CDAweb from February 27 to March 12, 2005. The time resolution is 1 min. **a** The variation of the solar wind density, **b** the variation of the solar wind flow speed. **c**, **d** Represents the half day moving average and the first derivative of the speed. The vertical light blue line represents the day of the maximum value of the solar wind density and the enhancement of the solar wind velocity around the Earth's orbit

proton density and the flow speed of the solar winds, provided by CDAweb, from February 27 to March 12, 2005. In panels (a) and (b) in this figure, proton density becomes maximum and flow speed starts to increase at approximately March 6, as indicated by the vertical light blue line. Moreover, the sign of the first derivative of the solar wind, that is, the acceleration of the flow speed, also inverted from negative to positive, as shown in panel (d). This feature is one of the characteristics of the stream interfaces of CIRs that arrive around Earth's orbit. We selected solar wind data and the geomagnetic indices of 7 days before and after the day in which the solar wind speed started to increase at the maximum density around the event dates described in the referenced CIR and SIR list. After that, we estimated the median value of the half-day averaged CH area, 1-h averaged solar wind, the IMF, and the geomagnetic indices (AL, AU, and SYM-H) by conducting

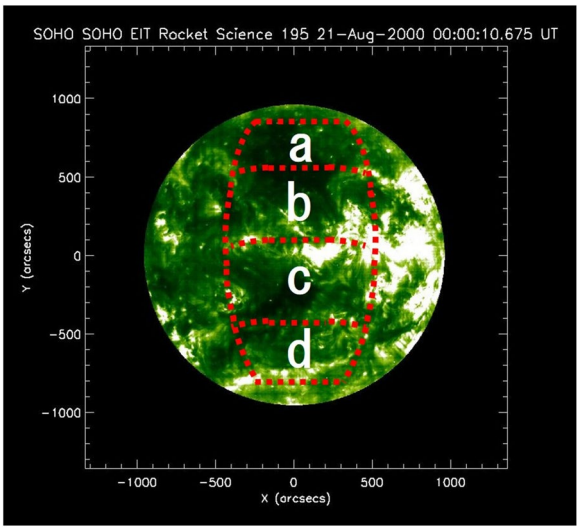

Fig. 2 The image of dividing four regions in Sun while surface

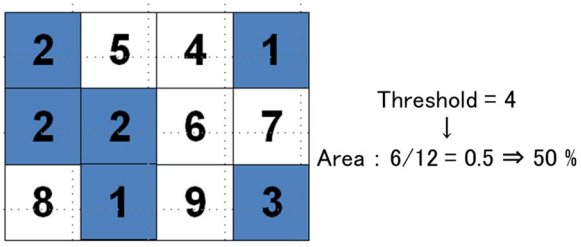

Fig. 3 Diagram of determining CH area. Pixels less than threshold are painted in blue

a superposed epoch analysis for solar cycles 23 (1996–2008) and 24 (2009–2016).

Identification of CH area on the solar surface

This section describes the identification of CH area from the EIT and AIA data. In the first step, we divided the solar surface into four regions: (−60 to −30, −30 to 30), (−30 to 0, −30 to 30), (0 to 30, −30 to 30), and (30 to 60, −30 to 30) degrees in solar latitude and longitude, respectively, as shown in Fig. 2. In the next step, we defined a threshold for solar brightness in the extreme ultraviolet (EUV) range as half of the median value of the intensity in a whole area using the method proposed by Akiyama et al. (2013). Lastly, we derived the CH area as the ratio of the number of pixels with a lower intensity than the threshold in each region. Figure 3 shows a schematic of how to determine the CH area. All pixel numbers are 12, and we set the threshold to 4 in this example. The value of the blue pixels is smaller than the threshold. The number of blue pixels is 6 in Fig. 3. Therefore, the area value is calculated as 6/12 = 0.5 = 50% in this schematic. Figure 4 shows an example of a CH region identified using this method. The identified CH regions in this analysis are shown in the part surrounded by the yellow line. The half-day averaged CH area was used in our analyses.

Classification of the orientation of the IMF associated with CIR events

The energy of solar wind flows is injected into the magnetosphere via the reconnection of the southward IMF and the terrestrial magnetic field. Therefore, in space weather applications, we are most interested in the solar wind's velocity and mass density and the strength and orientation of the interplanetary magnetic field (Russell 2001). In this study, we classified the patterns in the temporal variations in the IMF related to CIRs into four types. We first defined the cases in which IMF Bx and By are, respectively, positive and negative as "toward" cases. On the other hand, the cases in which IMF Bx and By are, respectively, negative and positive were defined as "away" cases. We further divided these into two groups containing either positive or negative IMF Bz for both the "toward" and "away" cases. Figure 5 shows the definition of the orientation of each component of the IMF in the GSM coordinate system.

Results

CH areas for solar cycles 23 and 24

Figures 6 and 7 show the CH area (percentage) obtained by conducting the superposed epoch analysis for solar cycles 23 and 24, respectively. Figure 6 shows the temporal variations of the 12-h averaged CH area (percentage) in the middle- and low-latitude regions during solar cycles 23 (1996–2008) and 24 (2009–2016) indicated by the black and red lines, respectively. The horizontal axis represents the time interval from −7 to 6 days before and after the solar wind velocity began to increase. The vertical dashed line indicates the start time of an enhancement of solar wind flow velocity. Error bars correspond to 95% confidence intervals with median absolute deviation (MAD). MAD is defined as the median of the absolute deviation from the median of the data set. In panel (c) in Fig. 6, the CH area in the low-latitude region in the southern hemisphere shows a clear increase before the arrival of high-speed solar wind for both solar cycles 23 and 24. The CH area in this region had a maximum value of about 5% and 3% for solar cycle 23 and 24, respectively. After that, those maximum values decreased to 1% within 3 days. On the other hand, as shown in panels (a), (b), and (d), the middle-latitude CH area did not exhibit a clear variation for solar cycle 23, and the CH areas in

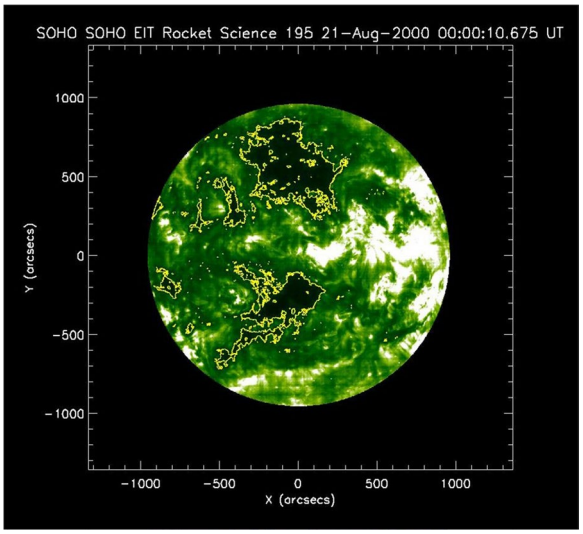

Fig. 4 The two-dimension solar image obtained from SOHO/EIT 195 Å on August 21, 2000. The identified CH in the present study are regions surrounded by a yellow line

these three sectors were smaller than those during solar cycle 24. The maximum value of these CH areas for solar cycle 24 was approximately 3%. Figure 7 shows the temporal variations of the average CH areas of the middle- to low-latitude regions using data from every two years for solar cycles 23 and 24. In the left panel (c), the low-latitude CH area in the southern hemisphere from 2002 to 2003 (the green line) shows a significant increase of 20.3%. The CH area began to increase significantly 4 days before the start time of the increase in solar wind speed. CH area exhibited a peak value half a day before the onset of an increase in solar wind speed. This time difference can be interpreted via the spiral structure of solar wind and the longitudinal width of the analysis window in the present study. The width of the window used was from −30° to 30° in solar longitude. Furthermore, the magnetic field lines of CHs form an angle of 45° with respect to the *x* axis of the GSM coordinate system. From these facts, we can determine that the Sun rotates 75° before the solar wind flow reaches Earth's orbit. Therefore, it takes 360°/75° = 4.8 days for a solar wind flow originated from a CH to arrive at Earth's orbit. However, CH area decreased by 10.7% 2 days after the solar wind began to increase, and then the CH area increased by 16.5% 4 days after the start time of the increase in solar wind speed. As shown in the left panels (b) and (c), the variation of the CH area in the latitude from −30° to 0° tended to be larger than that in the latitude from 0° to 30° for solar cycle 23. This tendency can also be seen for solar cycle 24, as shown in the right panels (b) and (c). Furthermore, the CH areas from 2013 to 2014 and from 2015 to 2016 significantly increased in the southern hemisphere, as shown in the right panels (c) and (d).

Relationship between CH area and solar wind speed

Figure 8 shows a scatter plot of the maximum value of CH area and solar wind speed for cycles 23 and 24. The horizontal and the vertical axes represent CH area and solar wind speed, respectively. The black line represents a linear regression. It should be noted that the values of the maximum CH areas in this figure are half of the sum of the CH area for area b (0° to 30° in solar latitude) and area c (−30° to 30° in solar latitude) in Fig. 6. In other words, Fig. 8 shows the correlation between the CH area from −30° to 30° in solar latitude and solar wind speed. The maximum values of the CH area for solar cycles 23 and 24 were 68.27% and 32.36%, respectively. The maximum solar wind speed values for solar cycles 23 and 24 were

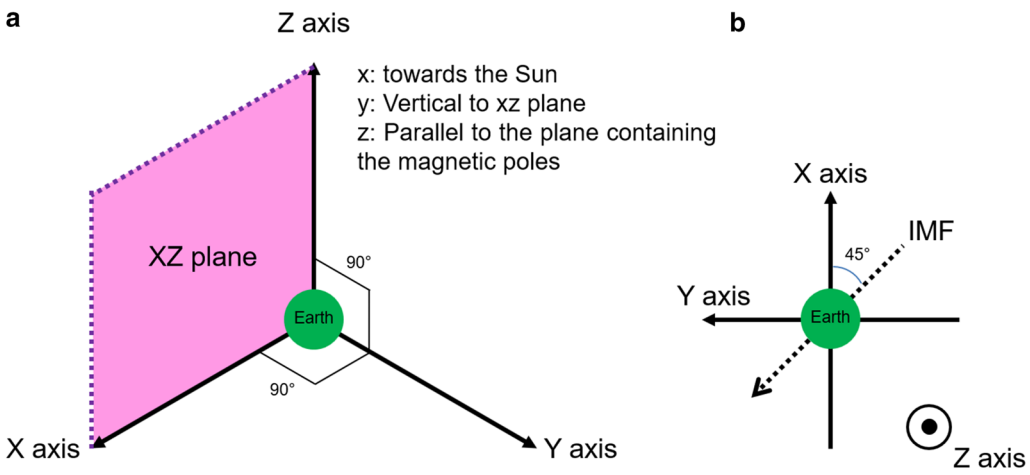

Fig. 5 The definition of orientation of each component of IMF. **a** The definition of geocentric solar magnetospheric (GSM) coordinate. The *x* axis is defined in the direction toward the Sun. The *z* axis is parallel to the plane containing the magnetic pole of the Earth. The *y* axis is vertical to the xz plane. **b** A view of the earth from the *z* axis direction. When viewed from the Earth, the IMF makes an angle of 45° with the *x* axis

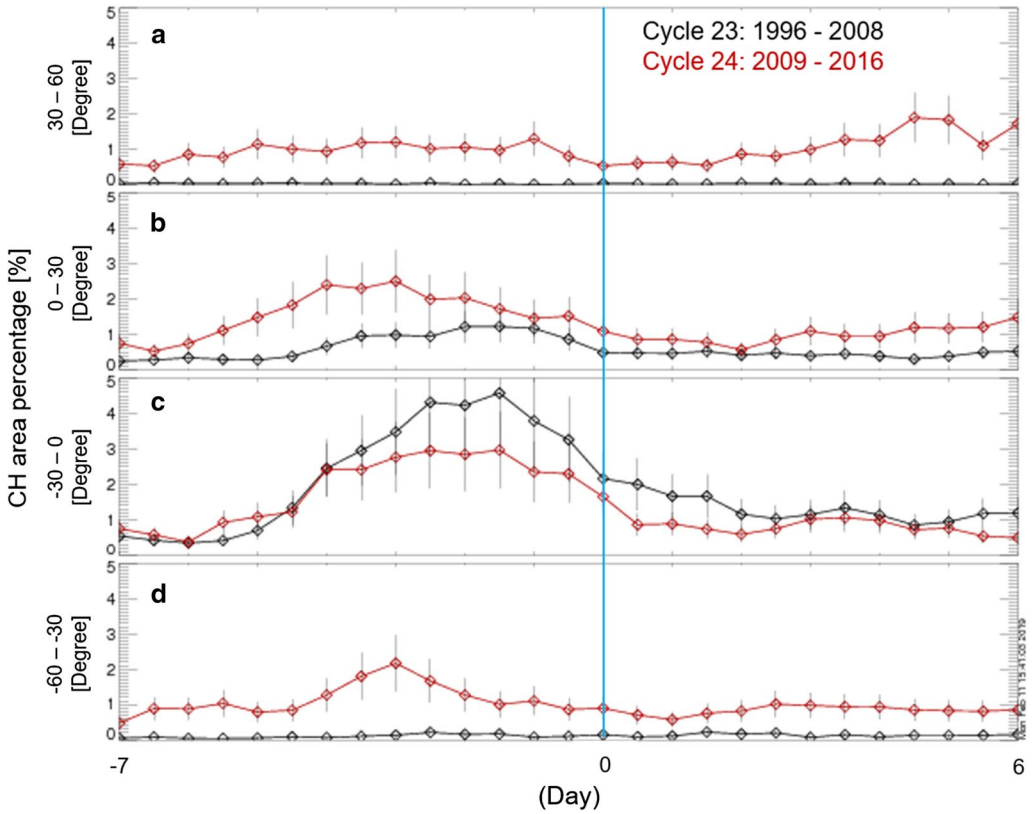

Fig. 6 Temporal variations of 12-h average CH area in the four latitudinal ranges for 13 days. The black and red lines correspond to the CH areas of solar cycle 23 (1996–2008) and 24 (2009–2016), respectively. The vertical light blue line represents the start time of an enhancement of solar wind velocity around the Earth's orbit. The left labels "Area a," "Area b," "Area c," and "Area d" in each panel show the regions of (30–60, − 30 to 30), (0–30, − 30 to 30), (− 30 to 0, − 30 to 30), and (− 60 to 30, − 30 to 30) degrees in the solar latitude and longitude, respectively

915.35 km/s and 790.58 km/s, respectively. As shown in Fig. 8, there is a positive correlation between the maximum values of CH area and solar wind speed for both solar cycles, and the correlation coefficients between the maximum values of CH area and solar wind speed for solar cycles 23 and 24 were 0.24 and 0.42, respectively. The covariance between the maximum value of CH area and solar wind speed was 246.51 in cycle 23 and 208.18 in cycle 24. Therefore, the data distribution was larger for solar cycle 23 than for solar cycle 24.

Variations of solar wind parameters and geomagnetic indices

The temporal variations of the solar wind parameters and the geomagnetic indices calculated through superposed epoch analyses for solar cycles 23 and 24 are shown in Figs. 9 and 10. These data were 12-h running-averaged in order to grasp the trend of the variations more visually. The vertical dashed line indicates the start time of an increase in solar wind flow velocity. The meaning of the horizontal axis is the same as that of Fig. 6. Solar wind speed started to increase approximately half a day before solar wind density became maximum in all cases for both solar cycles 23 and 24. This feature suggests that the stream interfaces of CIRs correspond to an increase in the solar flow speed and a decrease in density, as reported by Kataoka and Miyoshi (2006).

The variations of solar wind density, flow speed, and the IMF exhibited the same tendency in all cases for solar cycles 23 and 24, respectively. Solar wind density became maximum around the day in which solar wind speed increased and then decreased after 1 or 2 days. Solar wind speed became maximum within 2 days and decreased gradually after several days. However, the decreases in solar wind speed from the peaks for solar cycle 24 were faster than those for solar cycle 23. The sign of the IMF reversed approximately 1 day before the day in which solar wind speed increased, but the sign of the IMF in the "toward" cases with a positive IMF Bz only reversed after two or more days before the day in which solar wind speed increased. The daily variation of IMF Bz was larger than that of IMF Bx and By. Furthermore, the variations of the three magnetic indices after solar wind speed increases in cases with a negative IMF Bz were

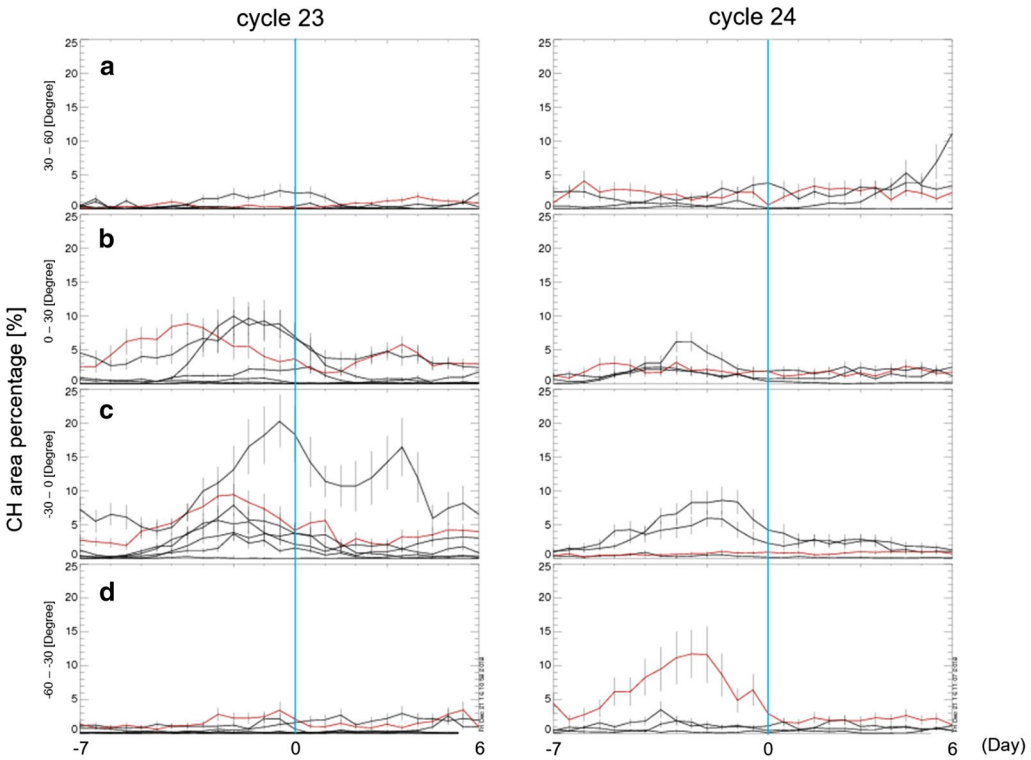

Fig. 7 Variation of the average CH area in the middle- to low-latitude regions with the data of every 2 years during solar cycle 23 (left panel) and 24 (right panel). The vertical light blue line represents the start time of an enhancement of solar wind velocity around the Earth's orbit. Red lines in both panels indicate the variation of the period of the solar maximum, from 2000 to 2001 (the left panel) and from 2013 to 2014 (the right panel)

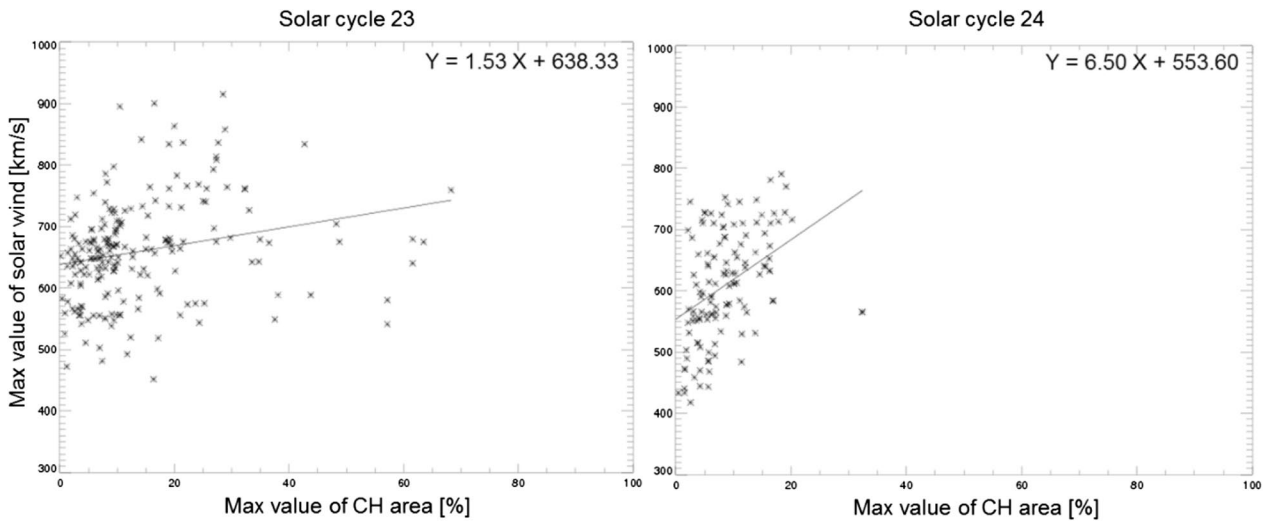

Fig. 8 The scatter plot of the maximum value of CH area and the maximum value of solar wind speed in cycles 23 and 24. The horizontal and vertical axis represents the CH area and the solar wind speed, respectively. The black line is a linear regression line

larger than those in cases with a positive IMF Bz. The variations of AU and AL roughly corresponded to the variation of IMF Bz.

On the other hand, the IMF cases with the largest variations in solar wind and magnetic indices were different between solar cycles 23 and 24. The maximum values for solar wind speed and the AU index for solar cycle

23 were larger than those for solar cycle 24 for all IMF cases, but those of solar wind density, AL, and SYM-H indices for solar cycle 24 were larger than those for solar cycle 23 depending on each IMF case. The peak values of the solar-density negative IMF Bz for solar cycle 24 were larger than those for solar cycle 23. Moreover, the minimum values of the AL and SYM-H indices for solar cycle 24 were larger than those for solar cycle 23 in the "toward" cases for either positive or negative IMF Bz.

The temporal variations of the AE and SYM-H indices for solar cycles 23 and 24 are shown in Figs. 11 and 12. Figure 11 shows the 12-h running-averaged variations of the AE index for IMF cases. The black and red lines indicate the variation of the AE index for solar cycles 23 and 24, respectively. The error bars represent standard deviation. The meanings of the vertical blue line and the horizontal axis are same as those for Fig. 6. The AE values shown in Fig. 11 were calculated by subtracting AL from AU; they do not show the observed value. As shown in this figure, the value of AE increased on the day the solar wind speed increased in each solar cycle. The maximum value of AE was 350.95 in the "toward" case and a negative IMF Bz for solar cycle 23. The variation of AE after the day in which solar wind speed began to increase (indicated by the blue vertical line) for cycle 23 tended to be larger than that for solar cycle 24 in all IMF cases, and this tendency was most remarkable in the "away" case with a positive IMF Bz. The peak AE value also tended to be larger in cases with a negative IMF Bz than those with a positive one. On the other hand, Fig. 12 shows the 12-h running-averaged variation of the SYM-H index for IMF cases. The black and red lines indicate the variation of the SYM-H index for solar cycles 23 and 24, respectively. The error bars represent standard deviation. The meanings of the vertical blue line and the horizontal axis are same as those for Fig. 6. As shown in this figure, the value of SYM-H decreased within half a day from the day in which solar wind speed increased for both solar cycles. The minimum value of SYM-H was −26.94 in the "away" case and for a negative IMF Bz in solar cycle 23. The variation of SYM-H after the beginning of the increase in solar wind speed for cycle 23 tended to be larger than that for solar cycle 24 in all IMF cases, and this tendency was most noticeable in the "away" case with a positive IMF Bz. These results are the same as those for AE. Moreover, the minimum value of SYM-H tended to be larger in the cases with a negative IMF Bz than with a positive one.

Discussion

Latitude of appearance of CH areas for solar cycles 23 and 24

The present study shows that the averaged variation of the CH area in the latitude range from 0° to 30° in the southern hemisphere was maximum during solar cycle 23 and that this tendency was remarkable from 2002 to 2003. Our results regarding this the north–south asymmetry of CH appearance are basically consistent with those shown by McIntosh et al. (2015) and Lowder et al. (2016), but we newly found that this asymmetry was strongest from 2002 to 2003 after the starting time of a declining phase. Moreover, Lowder et al. (2016) showed that the CH distribution in the latitude range from −55° to −30° was larger than that in the latitude range from −30° to 0° in 1996–2008 (see panel (b) in Fig. 2 in Lowder et al. (2016)). This tendency was not seen in the present results. This difference originates from the fact that we extracted the CHs related to CIRs for solar cycle 23, which were determined from solar wind data. According to Abunina et al. (2013, 2015), the origin of the high-speed solar winds observed near Earth's orbit is thought to be low-latitude or transequatorial CHs. Therefore, it can be assumed that the present data analysis method tends to select low-latitude CHs.

On the other hand, the present data analysis results also show that the characteristics of the CH appearances were different between solar cycles 23 and 24. CHs during solar cycle 24 tended to appear in a wider latitude region, between −30° and 30°, compared with those during solar cycle 23. However, the north–south asymmetry in CH appearance could also be seen during solar cycle 24. Recently, Bagashvili et al. (2017) reported that larger CHs frequently appeared in the southern hemisphere from 2013 to 2015. Their results are in good agreement with the increase in CH variation from 2013 to 2016 shown in Fig. 7. The important objective of the present study was to clarify the difference between the two solar cycles in terms of the latitude distribution of CHs that affect geomagnetic activity. The difference found is that the isolated CHs in solar cycle 23 tended to appear in a confined region of the southern hemisphere, whereas CHs in solar cycle 24 tended to appear in a wider region in the poloidal direction compared with those in solar cycle 23.

Relationship between CH area and solar wind speed

The results of the present study show that there is a positive correlation between the maximum values of CH area and solar wind speed for cycles 23 and 24. These maximum values were larger for solar cycle 23 than for solar cycle 24. This tendency indicates that solar wind speed in solar cycle 24 was lower than in solar cycle 23. The relationship between the maximum values of CH area and solar wind speed found in the present study is consistent with the results presented by Tokumaru et al. (2017), who indicated that there is a significant positive correlation between solar wind speed and the CH area. However,

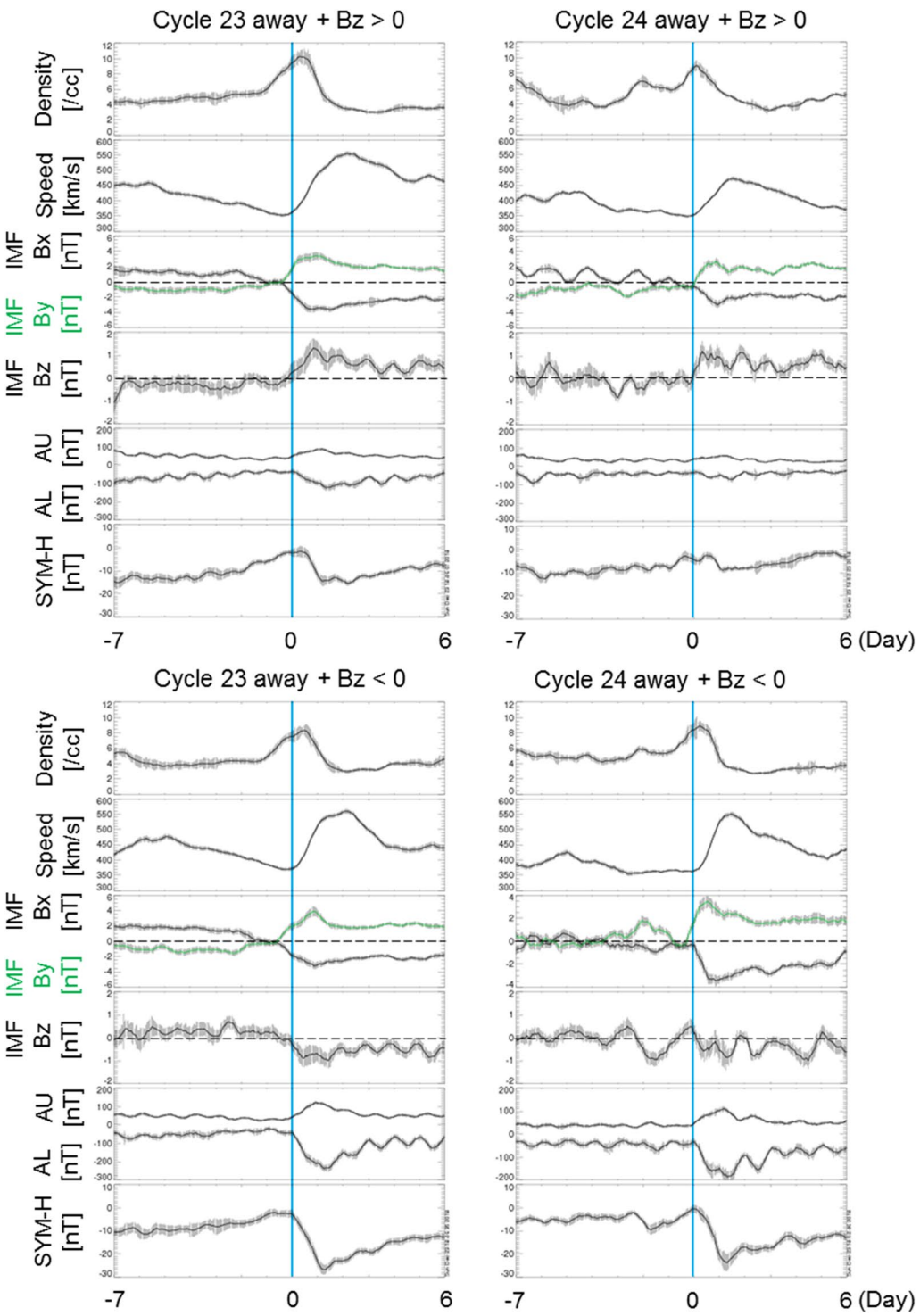

Fig. 9 Half-day averaged variation of solar wind proton density, solar flow velocity, and IMF, geomagnetic indices in the case of "away" (IMF Bx < 0 and By > 0) during solar cycle 23 and 24. The vertical light blue line represents the start time of an enhancement of solar wind velocity around the Earth's orbit. The error bar represents the standard deviation

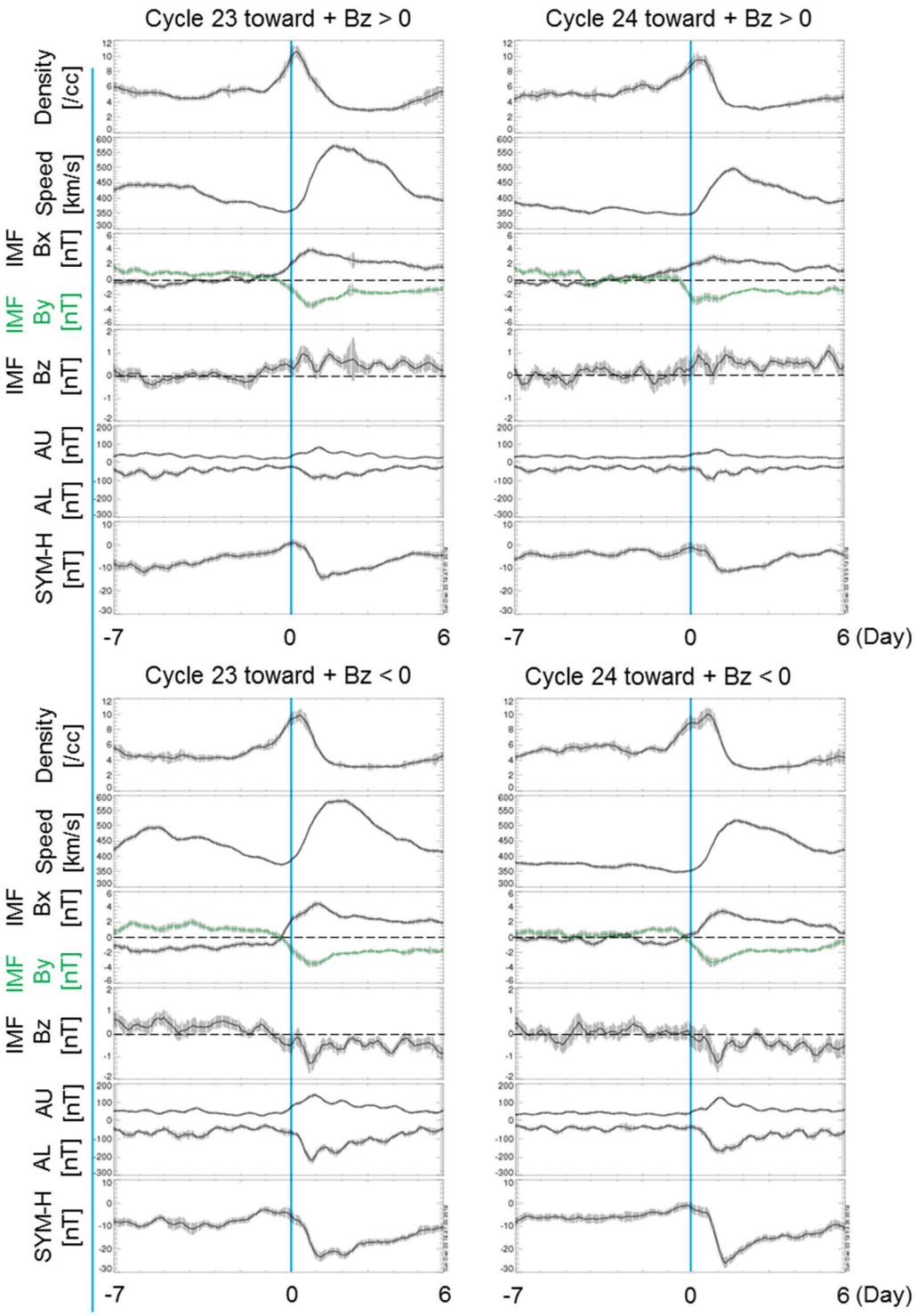

Fig. 10 Half-day averaged variation of solar wind proton density, solar flow velocity, and IMF, geomagnetic indices in the case of "toward" (IMF Bx > 0 and By < 0) during solar cycle 23 and 24. The vertical light blue line represents the start time of an enhancement of solar wind velocity around the Earth's orbit. The error bar represents the standard deviation

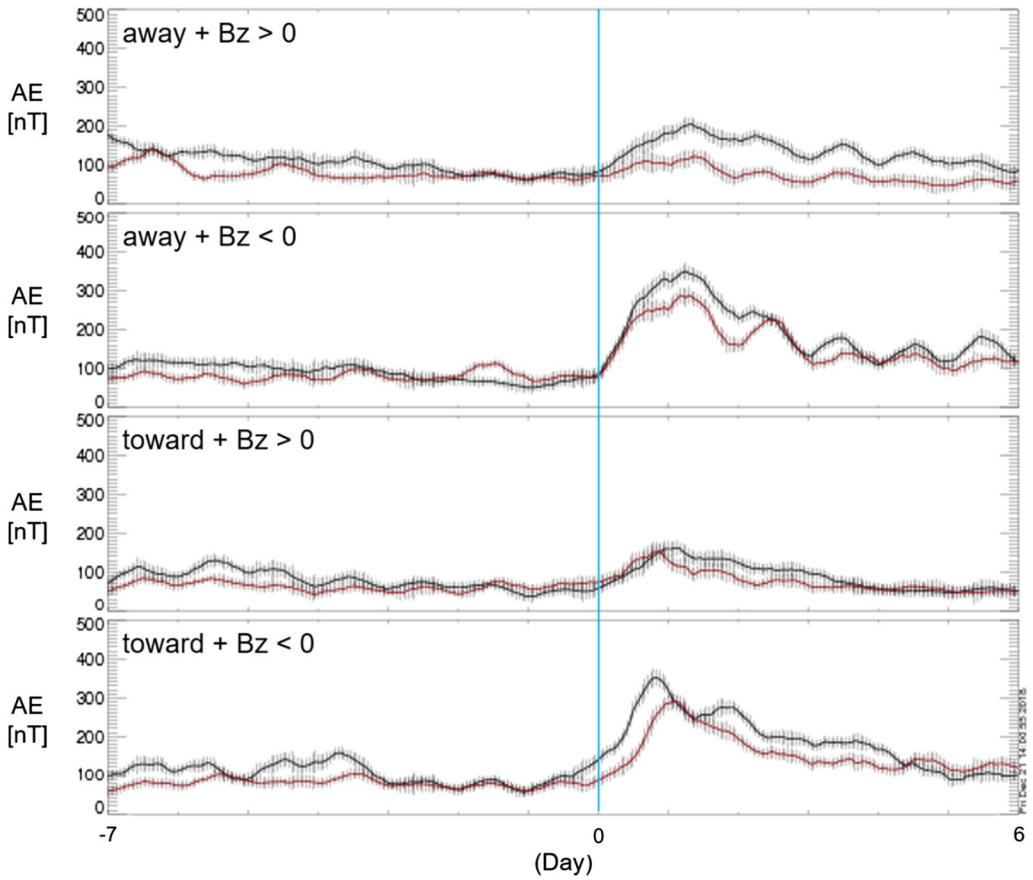

Fig. 11 The variation of AE index for IMF cases for solar cycle 23 (black line) and for cycle 24 (red line). The vertical light blue line represents the start time of an enhancement of solar wind velocity around the Earth's orbit. The error bar represents the standard deviation

they showed the relationship between the square root of CH area and solar wind speed. From these results, the differences in the relationship between CH area and solar wind speed for solar cycles 23 and 24 can be interpreted. The CH area for solar cycle 23 tended to be relatively large, and faster solar winds flowed out from the CHs. On the other hand, the CH area for solar cycle 24 tended to be relatively small compared with that for solar cycle 23. Therefore, the solar wind speed associated to CHs for solar cycle 24 was statistically lower than that for solar cycle 23.

Knowing the relationship between CH area and solar wind speed is valuable partly because it provides important information to elucidate the acceleration mechanism of solar winds and partly because it enables us to predict solar wind speeds at Earth from CH imaging observations. This relationship has been studied from the perspective of space weather forecast using many instruments (e.g., Vršnak et al. 2007; Rotter et al. 2012, 2015; Reiss et al. 2016; Tokumaru et al. 2017).

Variations of solar wind parameters and geomagnetic indices

The present study shows that the variations in solar wind and geomagnetic activity for solar cycle 24 tended to be smaller than those for solar cycle 23. In particular, this tendency can be seen in the variations of the AE index for solar cycles 23 and 24 in all IMF cases, as shown in Fig. 11. From those results, we conclude that the geomagnetic activity in solar cycle 24 associated with CIRs is moderate compared with that in solar cycle 23. Gopalswamy et al. (2015a) and Watari (2017) showed that geomagnetic activity was lower in solar cycle 24 than in solar cycle 23. The results of these previous studies are similar to our analysis results. Gopalswamy et al. (2015a) reported that the number of the magnetic storms was low because of the expansion of the CME due to the drop in solar wind density of 1 AU from 2008 to 2013. Watari (2017) said that the measured low geomagnetic activity was caused by the weak dawn-to-dusk solar wind electric field, which is a result of solar wind speed and

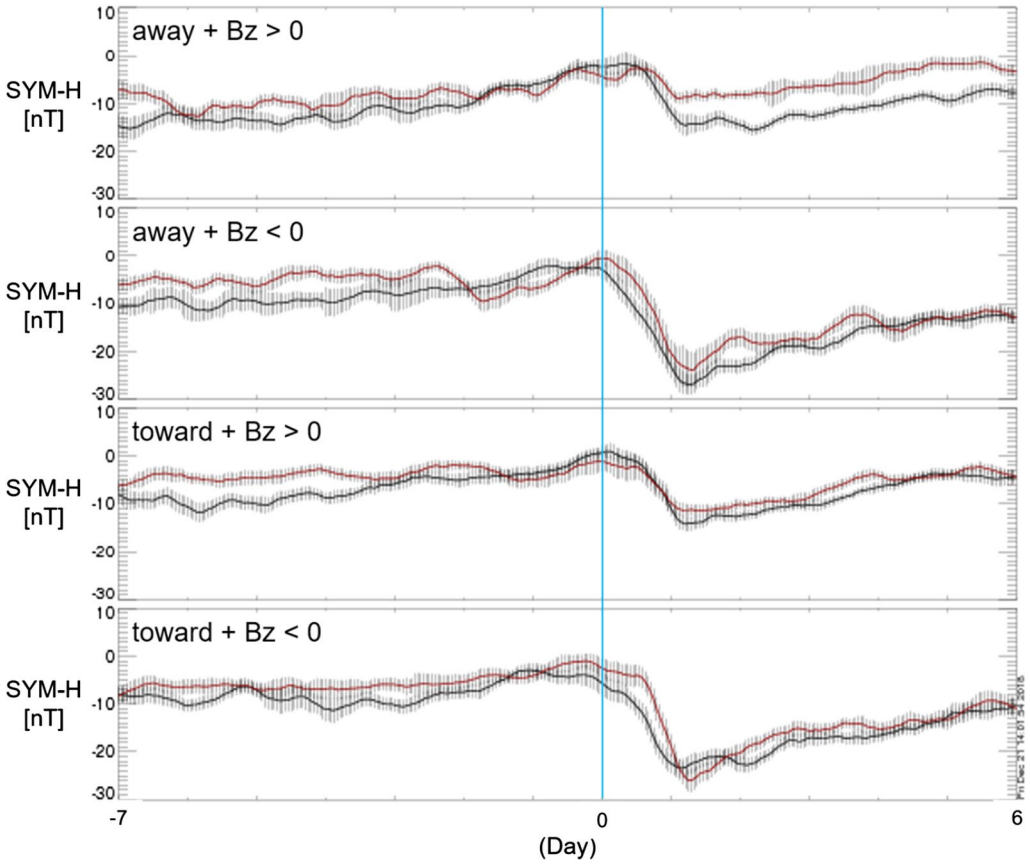

Fig. 12 The variation of SYM-H index for IMF cases for solar cycle 23 (black line) and for cycle 24 (red line). The vertical light blue line represents the start time of an enhancement of solar wind velocity around the Earth's orbit. The error bar represents the standard deviation

the north–south component of the solar wind magnetic field. The present study shows that the solar wind speeds for solar cycle 24 were lower than those for solar cycle 23. Therefore, it can be inferred that the intensity of the dawn-to-dusk electric field became weaker in solar cycle 24, as mentioned by Watari (2017). The most important result of the present study is that the variations of solar wind speed and the AU index for solar cycle 24 were smaller than those for solar cycle 23 in all IMF cases.

It should be noted that the number of CIR events analyzed for solar cycle 24 was lower than that for solar cycle 23 and that data after 2017 were not included in the present study. Therefore, it is necessary to increase the number of CIR events analyzed for solar cycle 24 and to analyze data from after 2017 in future works.

Conclusion

High-speed solar winds flow out from low-latitude CHs and have a significant influence on Earth's magnetosphere and ionosphere. Therefore, investigating the characteristics of the distribution of CH area and the variation of solar wind parameters and geomagnetic activity is important for space weather researches. We studied the temporal and spatial variations of the CH area related to high-speed solar winds observed around Earth's orbit for solar cycles 23 (1996–2008) and 24 (2009–2016). In addition, we performed a statistical analysis of the temporal variations of solar wind density, flow speed, the IMF, and geomagnetic indices and statistically investigated the relationship between low-latitude CHs, solar wind speeds, and geomagnetic activity for solar cycles 23 and 24. The results of this study are summarized below:

1. The variation of the CH area in the latitude range from 0° to 30° in the southern hemisphere was maximum for solar cycle 23, and CH areas did not appear in the middle-latitude region (30°–60°) in both hemispheres.
2. The north–south asymmetry of the low-latitude CH area was strongest from 2002 to 2003 after the start time of a declining phase in solar cycle 23.

3. The low-latitude CH area for solar cycle 24 appeared with north–south asymmetry just as for solar cycle 23. In addition, the CH area for solar cycle 24 tended to appear in a wider latitude region compared with that for solar cycle 23.
4. There is a positive correlation between the maximum values of CH area and solar wind speed. These maximum values were larger for solar cycle 23 than for solar cycle 24.
5. The variations of solar wind speed and the geomagnetic indices (AE and SYM-H) associated with CIRs for solar cycle 24 tended to be smaller than those for solar cycle 23, and the geomagnetic activity for solar cycle 24 associated with CIRs was moderate compared with that for solar cycle 23.

It should be noted that the results for solar cycle 24 shown in the present study are not absolutely representative because the data of the last part of the decline and solar-minimum data for solar cycle 24 are missing. Therefore, in future works, the number of CIR events for solar cycle 24 should be increased and data from after 2017 should be analyzed.

Abbreviations

CH: coronal hole; IMF: interplanetary magnetic field; CIR: corotating interaction region; SSN: sunspot number; WDC-SILSO: World Data Center for Sunspot Index and Long-Term Solar Observation; CME: coronal mass ejection; ULF: ultra-low frequency; HSS: high-speed stream; EIT: Extreme ultraviolet Imaging Telescope; SOHO: Solar and Heliospheric Observatory; AIA: Atmospheric Imaging Assembly; SDO: Solar Dynamics Observatory; GSM: geocentric solar magnetospheric; CDAweb: Coordinated Data Analysis Web; WDC, Kyoto: World Data Center for Geomagnetism, Kyoto University; IUGONET: Interuniversity Upper Atmosphere Global Observation NETwork; UDAS: IUGONET Data Analysis Software; SIR: stream interaction region; ACE: Advanced Composition Explorer; STEREO: Solar TErrestrial RElations Observatory.

Authors' contributions

YN wrote most of the manuscript. YN also designed the identification method for CH area and conducted all data analyses. AS and SN gave YN useful advice to improve the analyses. All authors read and approved the final manuscript.

Author details

[1] Graduate School of Evolution of the Universe and Earth, Ibaraki University, 2-1-1, Bunkyo, Mito 310-8512, Japan. [2] Ibaraki University, 2-1-1, Bunkyo, Mito 310-8512, Japan. [3] Institute for Space-Earth Environmental Research (ISEE), Nagoya University, Furo-cho, Chikusa-ku, Nagoya 464-8601, Japan.

Acknowledgements

This work is supported by JSPS KAKENHI Grant Numbers 26400478 and 16H06286. We used the EIT and AIA data provided by the Virtual Solar Observatory and AIA Cutoff Data, respectively. OMNI2 solar wind data were obtained from NASA's CDAweb. We also used the AU, AL, and SYM-H indices with a 1-min time resolution obtained from the World Data Center (WDC) for Geomagnetism, Kyoto University. We took advantage of the IUGONET (Inter-university Upper atmosphere Global Observation NETwork) database (IUGONET Type-A) and its data analysis software (UDAS). We would like to thank Editage (www.editage.jp) for English language editing. We acknowledge M. Yamaguchi for giving useful comments to improve the manuscript.

Competing interests

The authors declare that they have no competing interests.

Availability of data and materials

EIT data are available from the Virtual Solar Observatory (https://sdac.virtualsolar.org/cgi/search/). AIA data can be obtained from AIA Cutoff Data (https://www.lmsal.com/get_aia_data/). Solar wind data and geomagnetic indices were provided at the Coordinated Data Analysis Web (https://cdaweb.sci.gsfc.nasa.gov/). Geomagnetic indices are available from the World Data Center for Geomagnetism, Kyoto University (http://wdc.kugi.kyoto-u.ac.jp/).

Consent for publication

Not applicable.

Ethics approval and consent to participate

Not applicable.

Funding

This work is supported by JSPS KAKENHI Grant Nos. 26400478 and 16H06286.

Publisher's Note

Received: 10 October 2018 Accepted: 19 February 2019
Published online: 28 February 2019

References

Abunina M, Abunin A, Belov A, Gaidash S, Tassev Y, Velinov P, Mateev L, Tonev P (2013) Geoeffectivity of solar coronal holes with different magnetic field polarity, Bulgarian Academy of Sciences. Space Research and Technology Institute. Aerosp Res Bulg 25:70–77

Abunina M, Abunin A, Belov A, Eroshenko E, Gaidash S, Oleneva V, Yanke V, Kryakunova O (2015) On the influence of the coronal hole latitude and polarity on the geomagnetic activity and cosmic ray variations. In: Proceeding of Science, The 34th International Cosmic Ray Conference, 082

Akiyama S, Gopalswamy N, Yashiro S, Mäkelä P (2013) A study of coronal holes observed by SOHO/EIT and the Nobeyama radioheliograph. Publ Astron Soc Jpn 65:S15. https://doi.org/10.1093/pasj/65.sp1.s15

Altrock RC (2014) Forecasting the maxima of solar cycle 24 with coronal Fe xiv emission. Sol Phys 289:623–629

Alves MV, Echer E, Gonzalez WD (2006) Geoeffectiveness of corotating interaction regions as measured by Dst index. J Geophys Res 111:A07S05. https://doi.org/10.1029/2005ja011379

Bagashvili SR, Shergelashvili BM, Japaridze DR, Chargeishvili BB, Kosovichev AG, Kukhianidze V, Ramishvili G, Zaqarashvili TV, Poedts S, Khodachenko ML, Causmaecker P De (2017) Statistical properties of coronal hole rotation rates: Are they linked to the solar interior? Astron Astrophys 603:A134. https://doi.org/10.1051/0004-6361/201630377

Borovsky JE, Denton MH (2006) Differences between CME-driven storms and CIR-driven storms. J Geophys Res 111:A07S08. https://doi.org/10.1029/2005ja011447

Borovsky JE, Denton MH (2013) The differences between storms driven by helmet streamer CIRs and storms driven by pseudostreamer CIRs. J Geophys Res Space Phys 118:5506–5521. https://doi.org/10.1002/jgra.50524

Cranmer SR (2009) Coronal holes. Living Rev Sol Phys 6:3

Delaboudinière JP et al (1995) EIT: extreme-ultraviolet imaging telescope for the SOHO mission. Sol Phys 162:291–312

Gopalswamy N, Yashio S, Mäkelä P, Michalek G, Shibasaki K, Hathaway DH (2012) Behavior of solar cycles 23 and 24 revealed by microwave observations. Astrophys J Lett 750:L42

Gopalswamy N, Akiyama S, Yashiro S, Xie H, Mäkelä P, Michalek G (2015a) The mild space weather in solar cycle 24. Solar Stellar Astrophys. arXiv:1508.01603

Gopalswamy N, Tsurutani B, Yan Y (2015b) Short-term variability of the Sun–Earth system: an overview of progress made during the CAWSES-II period. Progr Earth Planet Sci 2:13. https://doi.org/10.1186/s40645-015-0043-8

Harvey KL, Recely F (2002) Polar coronal holes during cycles 22 and 23. Sol Phys 211:31–52

Harvey JW, Sheeley NR (1978) Coronal holes, solar wind streams, and geomagnetic activity during the new sunspot cycle. Sol Phys 59:159–173

Harvey K, Suess S, Aschwanden M, Guhathakurta M, Harvey J, Hathaway D, LaBonte B, Sheeley N, Tsurutani BT (2000) NASA white paper derived from workshop on coronal holes near solar maximum and over the solar cycle. NASA, Washington, DC

Hayashi H, Koyama Y, Hori T, Tanaka Y, Abe S, Shinbori A, Kagitani M, Kouno T, Yoshida D, Ueno S, Kaneda N, Yoneda M, Umemura N, Tadokoro H, Motoba T, the IUGONET Project Team (2013) Inter-university upper-atmosphere global observation NETwork (IUGONET). Data Sci J 12:WDS179–WDS184. https://doi.org/10.2481/dsj.wds-030

Jian L, Russell CT, Luhmann JG, Skoug RM (2006) Properties of stream interactions at one AU during 1995–2004. Sol Phys 239:337–392. https://doi.org/10.1007/s11207-006-0132-3

Jian LK, Russell CT, Luhmann JG (2011) Comparing solar minimum 23/24 with historical solar wind records at 1 AU. Sol Phys 274:321–344. https://doi.org/10.1007/s11207-011-9737-2

Jian LK, Russell CT, Luhmann JG, Galvin AB, Simunac KDC (2013) Solar wind observations at STEREO: 2007–2011. In: Proceedings of solar wind, American Institute of Physics, vol 1539, pp 191–194. https://doi.org/10.1063/1.4811020

Jiang J, Chatterjee P, Chouhuri AR (2007) Solar activity fore-cast with a dynamo model. Mon Not R Astron Soc 381:1527. https://doi.org/10.1111/j.1365-2966

Kamide Y, Kusano K (2013) Is something wrong with the present solar maximum? Space Weather 11:140–141. https://doi.org/10.1002/swe.20045

Kataoka R, Miyoshi Y (2006) Flux enhancement of radiation belt electrons during geomagnetic storms driven by coronal mass ejections and corotating interaction regions. Space Weather 4:S09004. https://doi.org/10.1029/2005SW000211

Lemen JR et al (2012) The atmospheric imaging assembly (AIA) on the solar dynamics observatory (SDO). Sol Phys 275:17–40. https://doi.org/10.1007/s11207-011-9776-8

Lowder C, Qiu J, Leamon R (2016) Coronal holes and open magnetic flux over cycles 23 and 24. Sol Phys 292:18. https://doi.org/10.1007/s11207-016-1041-8

Mcintosh SW, Leamon RJ, Krista LD, Title AM, Hudson HS, Riley P, Harder JW, Kopp G, Snow M, Woods TN, Kasper JC, Stevens ML, Ulrich RK (2015) The solar magnetic activity band interaction and instabilities that shape quasi-periodic variability. Nat Commun 6:6491. https://doi.org/10.1038/ncomms7491

Mordvinov AV, Yazev SA (2014) Reversals of the Sun's polar magnetic fields in relation to activity complexes and coronal holes. Sol Phys 289:1971–1981

Reiss MA, Temmer M, Veronig AM, Nikolic L, Vennerstorm S, Schöngassner F, Hofmeister S (2016) Verification of high-speed solar wind stream forecasts using operational solar wind models. Space Weather 14:495. https://doi.org/10.1002/2016SW001390

Rotter T, Veronig AM, Temmer M, Vršnak B (2012) Relation between coronal hole areas on the sun and the solar wind parameters at 1 AU. Sol Phys 281(2):793–813

Rotter T, Veronig AM, Temmer M, Vršnak B (2015) Real-time solar wind prediction based on SDO/AIA coronal hole data. Sol Phys 290(5):1355–1370

Russell CT (2001) Solar wind and interplanetary magnetic field: a tutorial. In: Song P, Singer HJ, Siscoe GL (eds) Space Weather, Geophysical Monograph 125. American Geophysical Union, Washington, DC, pp 73–89. https://doi.org/10.1029/gm125p0073

Schwenn R (2006) Space weather: the solar perspective. Living Rev Solar Phys 3:2. https://doi.org/10.12942/lrsp-2006-2

Selhorst CL, Gimenez de Castro CG, Válio A, Costa JER, Shibasaki K (2011) The behavior of the 17 GHz solar radius and limb brightening in the spotless minimum XXIII/XXIV. Astrophys J 734:64–66. https://doi.org/10.1088/0004-637x/734/1/64

Sheeley NR Jr, Harvey JW (1981) Coronal holes, solar wind streams, and geomagnetic disturbances during 1978 and 1979. Sol Phys 70:237–249

Shibasaki K (2013) Long-term global solar activity observed by the Nobeyama Radioheliograph. Publ Astron Soc Jpn 65:17

Svalgaard L, Cliver EW, Kamide Y (2005) Sunspot cycle 24: smallest cycle in 100 years? Geophys Res Lett 32:L01104. https://doi.org/10.1029/2004GL021664

Tanaka Y, Shinbori A, Hori T, Koyama Y, Abe S, Umemura N, Sato Y, Yagi M, Ueno S, Yatagai A, Ogawa Y, Miyoshi Y (2013) Analysis software for upper atmospheric data developed by the IUGONET project and its application to polar science. Adv Polar Sci 24:231–240. https://doi.org/10.3724/SP.J.1085.2013.00231

Tokumaru M, Satonaka D, Fujiki K, Hayashi K, Hakamada K (2017) Relation between coronal hole areas and solar wind speeds derived from interplanetary scintillation measurements. Sol Phys 292:41. https://doi.org/10.1007/s11207-017-1066-7

Tsurutani BT, Gonzalez WD, Gonzalez ALC, Tang F, Arballo JK, Okada M (1995) Interplanetary origin of geomagnetic activity in the declining phase of the solar cycle. J Geophys Res 100(21):717–733

Tsurutani BT et al (2006a) Corotating solar wind streams and recurrent geomagnetic activity: a review. J Geophys Res 111:A07S01. https://doi.org/10.1029/2005ja011273

Tsurutani BT, McPherron RL, Gonzalez WD, Lu G, Sobral JHA, Gopalswamy N (2006b) Introduction to special section on corotating solar wind streams and recurrent geomagnetic activity. J Geophys Res 111:5. https://doi.org/10.1029/2006ja011745

Verbanac G, Vršnak B, Veronig A, Temmer M (2011a) Equatorial coronal holes, solar wind high-speed streams, and their geoeffectiveness. Astron Astrophys 526:A20. https://doi.org/10.1051/0004-6361/201014617

Verbanac G, Vršnak B, Živkovic S, Hojsak T, Veronig AM, Temmer M (2011b) Solar wind high-speed streams and related geomagnetic activity in the declining phase of solar cycle 23. Astron Astrophys 533:A49. https://doi.org/10.1051/0004-6361/201116615

Vršnak B, Temmer M, Veronig AM (2007) Coronal holes and solar wind high-speed streams: I. Forecasting the solar wind parameters. Solar Phys 240(2):315–330

Watari S (2017) Geomagnetic storms of cycle 24 and their solar sources. Earth Planets Space 69:70. https://doi.org/10.1186/s40623-017-0653-z

Watari S, Kato H, Yamamoto K (2015) Hit rate of space weather forecasts of the Japanese forecast center and analysis of problematic events on the forecasts between June 2014 and March 2015. Sun Geosph 10(2):163–171

Zhang Y, Sun W, Feng XS, Deehr CS, Fry CD, Dryer M (2008) Statistical analysis of corotating interaction regions and their geoeffectiveness during solar cycle 23. J Geophys Res 113:A08106. https://doi.org/10.1029/2008JA013095